PGO-LIOM: Tightly Coupled LiDAR-Inertial Odometry and Mapping via Parallel and Gradient-Free Optimization

Hongming Shen, Qun Zong, Bailing Tian, Xuewei Zhang, and Hanchen Lu

***Abstract*—Real-time localization and mapping for micro aerial vehicles (MAV) is a challenging problem, due to the limitation of the onboard computational power. In this article, a tightly coupled light detection and ranging (LiDAR)-inertial odometry is developed, which achieves high accuracy, real-time trajectories estimation for MAV utilizing only onboard sensors and a low-power onboard computer. The key idea of the proposed method is to integrate the IMU measurements, correct LiDAR matching measurements, LiDAR matching outliers into one nonlinear and noncontinuous objective function, and formulate the localization and mapping problem as a stochastic optimization problem. To deal with the nonlinear and noncontinuous objective function, a gradient-free optimization method is proposed to solve the stochastic optimization problem with a single parallel iteration. The novel constructed objective function and gradient-free optimization algorithm enable the proposed LiDAR-inertial odometry to achieve high accuracy and low time consumption. The effectiveness of the proposed method is demonstrated through various scenarios, including public datasets and real-world flight experiments.**

***Index Terms*—Aerial robots, LiDAR-based perception, parallel processing, sensor fusion, state estimation.**

I. Introduction

LOCALIZATION and mapping is a fundamental task in developing autonomous micro aerial vehicles (MAV). With the deployment of the autonomous MAV, it has the potential to enable surveillance, information gathering, and exploration. Both of these missions rely on reliable state estimation for MAV. During the last decade, the global navigation satellite system (GNSS) [1], motion capture systems [2], and ultra-wideband (UWB) [3] are well-applied for MAV-based applications. However, these navigation systems rely on external sensings are only functional under certain environmental conditions. For the real-world application, MAVs have to travel through a variety of diverse environments or operate in previously unknown unstructured rough terrain where external sensors are difficult to set up. With the goal of achieving a fully autonomous application for MAV in different scenarios flexibly, it is necessary to develop a real-time localization and mapping system that can work without external sensors. Thanks to the continuously reduced cost and weight of LiDAR in recent years, it has become a viable onboard sensing payload for MAV. Compared with visual navigation systems (VNS), LiDAR-based localization and mapping systems can provide more reliable state estimation thanks to the direct depth measurement, which is immune to scene illumination and texture changes. The aforementioned character is critical for the aerial platforms since they are easily destroyed when state estimation failures occur. Despite the above advantages, the large number point cloud generated by LiDAR worsens the computational complexity. Different from the ground vehicles, which are easy to take laptop, or even desktop onboard, a low-power onboard computer is the preference for MAV to improve its duration of the flight. Hence, a LiDAR-based navigation system that can provide real-time localization and mapping with a low-power onboard computer is crucial for autonomous MAV applications.

A. Related Work

Real-time localization and mapping is a challenging problem for LiDAR navigation systems (LNS). In [4], a portable LiDAR-based localization and mapping system is developed through the point cloud registration technology represented by iterative closest point (ICP) [5], generalized iterative closest point (GICP) [6], and normal distribution transformation (NDT) [7], which can provide pose estimation by the dense point cloud. Processing the dense point cloud is very computationally costly, with the aim of reducing the computational cost of [4], a voxelization strategy is adopted in LiTAMIN [8] and LiTAMIN2 [9] to downsample a large number of the raw point cloud, and a high-performance graphics processing unit (GPU) is used to accelerate the localization and mapping procedure. However, different from the low-power GPU preferred by MAVs, the high-performance GPU is difficult to take onboard, due to the power

Manuscript received 23 March 2022; revised 7 September 2022 and 17 November 2022; accepted 4 December 2022. Date of publication 20 December 2022; date of current version 8 May 2023. This work was supported in part by the National Key Research and Development Program of China under Grant 2018AAA0102401, in part by the National Natural Science Foundation of China under Grant 62073234, Grant 62022060, Grant 61873340, Grant 62273249, and in part by the Integration of Industry, Education and Research Innovation Fund of China University under Grant 2021ZYA08009. *(Corresponding author: Bailing Tian.)*

The authors are with the School of Electrical and Information Engineering, Tianjin University, Tianjin 300072, China (e-mail: shenhm@tju.edu.cn; zongqun@tju.edu.cn; bailing_tian@tju.edu.cn; zhangxuewei@tju.edu.cn; luhanchen_1993@tju.edu.cn).

Color versions of one or more figures in this article are available at https://doi.org/10.1109/TIE.2022.3229329.

Digital Object Identifier 10.1109/TIE.2022.3229329

and weight limitation of MAVs. In DLO [10], a lightweight LNS is developed through the GICP matching method in the context of the DARPA Subterranean Challenge. DLO enables the use of dense point cloud to provide real-time pose estimation for MAV, through the pruning of GICP matching with an adaptive keyframe strategy. Nonetheless, the keyframe strategy is a trade-off between accuracy and real-time performance. Feature-based LNS extracts geometric features from LiDAR scans to improve the real-time performance without sacrificing localization and mapping accuracy. LOAM [11] is a popular localization and mapping algorithm, which can provide low-drift pose estimation and mapping. Simple geometric feature extraction strategies are introduced in LOAM, where the feature points are segmented into edge features and planar features based on local smoothness, and the robot pose is estimated by doing edge-to-edge and planar-to-planar matching procedure. However, LiDAR-only localization and mapping methods will struggle to perform robustly during high-speed motion. Therefore, LiDAR is typically fused with an IMU for robust localization and mapping. LIMO [12], a tightly-coupled LiDAR-inertial odometry, introduced a bundle adjustment (BA) into LNS to jointly optimize measurements from LiDAR and IMU. Although BA has good performance in the VNS field, for LiDAR odometry which has 10–100 times of feature points than the visual odometry, BA is designed to process all the LiDAR features in the local window, the real-time performance is difficult to achieve by onboard computing power. With the aim of improving the real-time performance of the BA process performed in LIOM [12], LINS is presented in [13], which uses an error-state Kalman filter to fuse the measurements from LiDAR and IMU in a tightly coupled manner. In LIO-SAM [14], one of the state-of-the-art LiDAR-inertial odometry is proposed by fusing the IMU preintegration factor and scan-to-map matching factor into a factor graph, which can achieve real-time with onboard computing power thanks to the keyframe strategy. In CLINS [15], a continuous time LiDAR-inertial system is proposed by adopting a nonrigid registration using B-splines. With the aim of achieving localization and mapping for autonomous MAV, FAST-LIO is presented in [16], a Sherman–Morrison–Woodbury equation is adopted to reduce the computation complexity of the iterated extended Kalman filter (IEKF) update procedure. To further improve the real-time performance of FAST-LIO, an incremental KD-tree [17] is implemented in FAST-LIO2 [18], which significantly improves the efficiency of LiDAR matching and mapping procedure.

B. Motivations and Contributions

In view of the aforementioned analysis, LiDAR-based localization and mapping generally adopt the voxelization method [8], [9], keyframe strategy [10], [14], effective data structures [18] to improve LiDAR matching efficiency and solve the localization and mapping problem through nonlinear optimization or the Kalman filter. These methods are the Gaussian approximation of the maximum *a posteriori* (MAP) problem solved through the iterative least-squares optimization. Only correct LiDAR matchings are used in the aforementioned methods to make observations satisfying the Gaussian distribution assumption. However, discarded incorrect LiDAR matchings may help improve the accuracy, and the iterative process is time-consuming due to the data association procedure in each iterative. With the goal of designing a computationally efficient and high-accuracy localization and mapping system, in this work, a tightly coupled LiDAR-inertial odometry is developed with a single parallel-iteration solver. The key idea of the proposed method is to integrate the IMU measurements, correct LiDAR matching measurements, LiDAR matching outliers into one nonlinear and noncontinuous objective function, and formulate the localization and mapping problem as a stochastic optimization problem. With gradient-free optimization, the nonlinear and noncontinuous stochastic optimization problem is solved through a Monte-Carlo sampling in real-time. The main contributions of this article are listed as follows:

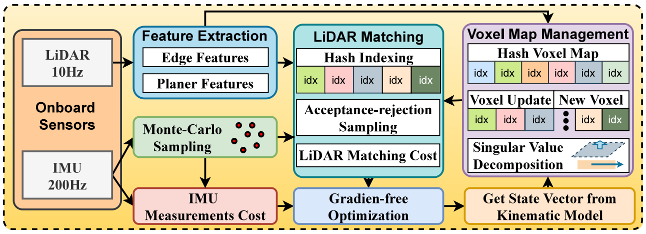

Fig. 1. System overview of the proposed LiDAR-inertial odometry.

1) A tightly coupled localization and mapping approach is proposed, which considers IMU measurements, the likelihood of correct LiDAR matchings, and the number of incorrect LiDAR matchings simultaneously.
2) To deal with the nonlinear and noncontinuous localization and mapping problem, a gradient-free optimization algorithm is proposed to solve the optimization with a single parallel iteration, which significantly improves the real-time performance of the localization and mapping process.
3) The proposed method is fully paralleled, which can provide real-time localization and mapping with low-power onboard computation power. Moreover, a real-world autonomous flight is performed to demonstrate the application of the proposed LiDAR-inertial odometry.

II. System Overview

A system overview of the proposed LiDAR-inertial odometry is given in Fig. 1, which takes advantage of measurements from LiDAR and IMU in a tightly coupled manner. The LiDAR point cloud measurements are fed into the feature extraction algorithm proposed in LOAM [11], which extracts features on edge and planer by calculating the curvature of each LiDAR point. In order to perform the LiDAR matching process, the extracted features are registered to a voxel map. The voxel map management module is in charge of maintaining a local map in a Hash table through the adaptive voxelization method [19] and the singular value decomposition (SVD) technique (see Section III-B). The LiDAR matching cost is constructed by formulating the LiDAR matching problem as a maximum likelihood estimation (MLE) problem (see Section IV-A2). Thanks to the acceptance–rejection sampling [20], which provides a criterion for judging whether a LiDAR matching is correct, the LiDAR matching cost considers the likelihood of correct matchings and the number of incorrect matchings simultaneously. To deal with the nonlinear and noncontinuous cost functions, a gradient-free optimization-based sensor fusion method is proposed to approximate the optimal solution through a fully paralleled Monte-Carlo sampling (see Section IV-B).

III. Problem Formulation

Consider a localization and mapping system, which is modeled by taking advantage of measurements from a LiDAR, and an IMU. The full state vector is defined as

$$\mathbf{x} = \left[\mathbf{t}^\top, \mathbf{v}^\top, \mathbf{R}^\top, \mathbf{b}_a^\top, \mathbf{b}_g^\top\right]^\top \tag{1}$$

where $\mathbf{t}$ is the translation vector, $\mathbf{v}$ is the velocity vector, $\mathbf{R} \in \mathrm{SO}(3)$ is the rotation matrix, $\mathbf{b}_a$ and $\mathbf{b}_g$ are IMU accelerometer and gyro biases, respectively.

Different from traditional LiDAR-inertial odometry, the present work solves the localization and mapping problem as a stochastic optimization problem.

$$\hat{\mathbf{u}} = \arg\min_{\mathbf{u}} \mathbb{E}_{\boldsymbol{\tau}\sim\mathcal{Q}}\left[\mathbf{S}(\mathbf{x}, \boldsymbol{\tau})\right] \tag{2}$$

where $\boldsymbol{\tau}$ is treated as a random vector generated by a Gaussian noise process $\boldsymbol{\tau} \sim \mathcal{Q}(\mathbf{u}, \boldsymbol{\sigma}_u)$, $\mathbf{u} = [\boldsymbol{\omega}^\top, \mathbf{a}^\top]^\top$, which includes the angular velocity $\boldsymbol{\omega}$ and local liner acceleration $\mathbf{a}$, is the mean vector of $\boldsymbol{\tau}$, and $\boldsymbol{\sigma}_u$ is the covariance matrix of $\boldsymbol{\tau}$. $\mathbb{E}_{\boldsymbol{\tau}\sim\mathcal{Q}}[\cdot]$ denotes the expectation operation over the random vector $\boldsymbol{\tau}$ with respect to $\mathcal{Q}$, which is abbreviated as $\mathbb{E}_{\mathcal{Q}}[\cdot]$ in the rest of this article. $\mathbf{S}(\mathbf{x}, \boldsymbol{\tau})$ is the cost function, which is constructed through IMU measurements residual $\mathbf{r}_I(\mathbf{x}, \boldsymbol{\tau})$ and LiDAR measurements residual $\mathbf{r}_L(\mathbf{x}, \boldsymbol{\tau})$

$$\mathbf{S}(\mathbf{x}, \boldsymbol{\tau}) = \mathbf{r}_I(\mathbf{x}, \boldsymbol{\tau}) + \mathbf{r}_L(\mathbf{x}, \boldsymbol{\tau}). \tag{3}$$

At time t_k, $\mathbf{S}(\mathbf{x}, \boldsymbol{\tau})$ is a function of the state vector $\mathbf{x}_{t_{k-1}}$ and the random vector $\boldsymbol{\tau}_{t_{k-1}}$. $\mathbf{x}_{t_{k-1}}$ is the state vector estimated at time t_{k-1}, which is a constant vector at time t_k. $\boldsymbol{\tau}_{t_{k-1}}$ is a random vector with a mean vector of $\mathbf{u}_{t_{k-1}}$. At time t_k, if the mean vector $\mathbf{u}_{t_{k-1}}$ can be solved from (2), the state vector $\mathbf{x}_{t_k}$ can be estimated by substituting $\hat{\mathbf{u}}_{t_{k-1}}$ and $\hat{\mathbf{x}}_{t_{k-1}}$ into the kinematic model (5).

A. Kinematic Model

The kinematic model is defined as follows:

$$\begin{aligned} &\dot{\mathbf{t}} = \mathbf{v}, \dot{\mathbf{v}} = \mathbf{R}\mathbf{a}, \dot{\mathbf{R}} = \mathbf{R}[\boldsymbol{\omega}]_\wedge \\ &\dot{\mathbf{b}}_{\boldsymbol{\omega}} = \mathbf{0}_{3\times1}, \dot{\mathbf{b}}_{\mathbf{a}} = \mathbf{0}_{3\times1} \end{aligned} \tag{4}$$

where $[\cdot]_\wedge$ denotes the skew-symmetric cross-product matrix. The state estimated at time t_k can be represented as a discrete-time kinematic model of the form

$$\mathbf{x}_{t_k} = F(\mathbf{x}_{t_{k-1}}, \mathbf{u}_{t_{k-1}}) \tag{5}$$

where $F(\cdot)$ denotes the state-transition funtion.

B. Map Representation

Following our previous work [21], an adaptive voxelization method [19] is adopted to maintain a local map for LiDAR-inertial odometry. The local map is divided into a set of voxels, each voxel containing a group of LiDAR points $\mathbf{p}_i (i = 1, \ldots, N)$ indexed in a Hash table. Assuming that each voxel $\mathbf{m}$ in the local map is subject to Gaussian distributions $\mathbf{m} \sim \mathcal{N}(\mathbf{m}^\mu, \boldsymbol{\sigma}_{\mathbf{m}})$

$$\begin{aligned} \mathbf{m}^\mu &= \frac{1}{N}\sum_{i=1}^{N}\mathbf{p}_i \\ \boldsymbol{\sigma}_m &= \frac{1}{N-1}\sum_{i=1}^{N}(\mathbf{p}_i - \mathbf{m}^\mu)(\mathbf{p}_i - \mathbf{m}^\mu)^\top \end{aligned} \tag{6}$$

where $\mathbf{m}^\mu$ and $\boldsymbol{\sigma}_m$ are mean and covariance matrix of the Gaussian distribution. The voxels in the local map can be divided into different shapes depending on the relationships between the eigenvalues of the covariance matrix $\boldsymbol{\sigma}_m$. A SVD is performed to calculate the eigenvalues of the covariance matrix $\boldsymbol{\sigma}_m$

$$\boldsymbol{\sigma}_{\mathbf{m}} = [\mathbf{V}_1, \mathbf{V}_2, \mathbf{V}_3]\begin{bmatrix} \lambda_1 & 0 & 0 \\ 0 & \lambda_2 & 0 \\ 0 & 0 & \lambda_3 \end{bmatrix}[\mathbf{V}_1, \mathbf{V}_2, \mathbf{V}_3]^\top \tag{7}$$

where λ_1, λ_2, and λ_3 are eigenvalues of the covariance matrix $\boldsymbol{\sigma}_{\mathbf{m}}$ in descending order. $\mathbf{V}_1, \mathbf{V}_2, \mathbf{V}_3$ are eigenvectors that correspond to λ_1, λ_2, λ_3, respectively.

Hence, voxels in the local map can be divided into following three categories.

1) *Plane voxel:* A voxel that satisfies $\lambda_2 \gg \lambda_3$. A plane voxel is represented by a centroid $\mathbf{m}^{\mu_p}$ and a normal vector $\mathbf{m}^{n_p} = \mathbf{V}_3$ of the plane.
2) *Edge voxel:* A voxel that is not a plane voxel and satisfies $\lambda_1 \gg \lambda_2$. An Edge voxel is represented by a centroid $\mathbf{m}^{\mu_e}$ and a normal vector $\mathbf{m}^{n_e} = \mathbf{V}_1$ of the edge.
3) *Candidate voxel:* A voxel that is neither a plane voxel nor edge voxel. Candidate voxel is not considered in cost function construction and needs more points to cluster plane voxel or edge voxel.

IV. Tightly Coupled LiDAR-Initial Odometry

A. Construction of the Cost Function

The state of the LiDAR-inertial odometry is estimated based on sensors observation. For the proposed tightly coupled LiDAR-inertial odometry, IMU measurements cost and LiDAR matching cost are considered, which are described in more detail as follows.

1) IMU Measurements Cost: The IMU measurements model is defined as follows:

$$\begin{aligned} \mathbf{a}_m &= \mathbf{a} + \mathbf{R}^\top\mathbf{g} + \mathbf{b}_a + \mathbf{n}_a \\ \boldsymbol{\omega}_m &= \boldsymbol{\omega} + \mathbf{b}_g + \mathbf{n}_g \end{aligned} \tag{8}$$

where $\mathbf{a}_m$ and $\boldsymbol{\omega}_m$ are raw IMU measurements, $\mathbf{g}$ is the constant gravity vector, $\mathbf{n}_a$ and $\mathbf{n}_g$ are the Gaussian white noise of acceleration and gyroscope measurements.

Thanks to the novel formulation in (2), the IMU measurements residual is defined in (9) instead of the complicated IMU preintegration formulation [22]

$$\mathbf{r}_I(\mathbf{x}, \boldsymbol{\tau}) = \left\| \begin{array}{c} \mathbf{a}_m - \hat{\mathbf{a}} - \hat{\mathbf{R}}^\top \mathbf{g} - \hat{\mathbf{b}}_a \\ \boldsymbol{\omega}_m - \hat{\boldsymbol{\omega}} - \hat{\mathbf{b}}_g \end{array} \right\|_2 . \tag{9}$$

For the gradient-free optimization described in Section IV-B, $\hat{\boldsymbol{\omega}}$ and $\hat{\mathbf{a}}$ are approximated through the Monte-Carlo sampling over $\boldsymbol{\tau}$.

2) LiDAR Matching Cost: The objective of the LiDAR matching process is to construct the state-dependent cost through geometric constraints between feature points and the voxel map. When a new LiDAR scan arrives, edge features and planer features are extracted by the algorithm proposed in [11]. The LiDAR matching problem can be formulated as a MLE problem given follows.

$$\begin{aligned} \hat{\mathbf{T}} &= \arg\max_{\mathbf{T}} \prod_{i=1}^{n} L\left(\mathbf{T}^B \mathbf{f}_i | {}^I\mathbf{M}\right) \\ &= \arg\min_{\mathbf{T}} \sum_{i=1}^{n} -\log\left(L\left({}^I\mathbf{f}_i | {}^I\mathbf{M}\right)\right) \end{aligned} \tag{10}$$

where $\mathbf{T} \in \mathrm{SE}(3)$ is the transformation matrix. n is the number of feature points in the current LiDAR scan. $L({}^I\mathbf{f}_i|{}^I\mathbf{M})$ represents the likelihood of observing a feature point ${}^I\mathbf{f}_i$ generated from the voxel map $\mathbf{M}$.

Inspired by [23], the likelihood function $L({}^I\mathbf{f}_i|{}^I\mathbf{M})$ can be simplified through the Gaussian mixture model (GMM)

$$L\left({}^I\mathbf{f}_i | {}^I\mathbf{M}\right) = L\left({}^I\mathbf{f}_i | {}^I\mathbf{m}_j\right) \tag{11}$$

where ${}^I\mathbf{m}_j$ is the voxel correspondence to feature ${}^I\mathbf{f}_i$, which is found through the feature-to-map matching (FMM) according to the hash indexing.

However, the hash indexing is a simple feature corresponding strategy, which may lead to a fraction of incorrect matchings. Introducing matching outliers into (10) can compromise the correctness of the resulting estimate. Hence, an acceptance-rejection algorithm [20] is adopted to refine the matching results. With the assumption that each voxel is subject to a Gaussian distribution, the target distribution is defined as

$$\begin{aligned} & f({}^I\mathbf{f}_i|{}^I\mathbf{m}_j) \\ & = \frac{1}{\left[(2\pi)^3 \left|\boldsymbol{\sigma}_{m,j}\right|\right]^{\frac{1}{2}}} \exp\left[-\frac{1}{2}\left({}^I\mathbf{f}_i - \boldsymbol{m}_j^{\mu}\right)^\top \boldsymbol{\sigma}_{m,j}^{-1}\left({}^I\mathbf{f}_i - \boldsymbol{m}_j^{\mu}\right)\right] . \end{aligned} \tag{12}$$

The upper bound of the target distribution $\bar{f}({}^I\mathbf{f}_i|{}^I\mathbf{m}_i)$ can be defined as

$$f({}^I\mathbf{f}_i|{}^I\mathbf{m}_j) \leq \bar{f}({}^I\mathbf{f}_i|{}^I\mathbf{m}_j) = \frac{1}{\left[(2\pi)^3 \left|\boldsymbol{\sigma}_{m,j}\right|\right]^{\frac{1}{2}}} . \tag{13}$$

Using the acceptance–rejection sampling for each feature point, the criterion for judging whether a feature point ${}^I\mathbf{f}_i$ is corresponding with a voxel ${}^I\mathbf{m}_j$ is defined as

$$c \leq \frac{f({}^I\mathbf{f}_i|{}^I\mathbf{m}_j)}{\bar{f}({}^I\mathbf{f}_i|{}^I\mathbf{m}_j)} \tag{14}$$

where $c \in [0, 1]$ is the acceptance–rejection threshold.

According to the MLE problem (10) and the LiDAR matching outlier criterion (14), the LiDAR matching cost is constructed based on the following twofold: 1) The likelihood of correct matchings, 2) the number of matching outliers. As noted in our previous work [21], the negative log-likelihood function $-\log(L({}^I\mathbf{f}_i|{}^I\mathbf{m}_j))$ can be simplified as point-to-voxel distance d_{p2v} using such a Gaussian approximation and principal component analysis (PCA). The LiDAR matching cost can be noted as

$$\mathbf{r}_L(\mathbf{x}, \boldsymbol{\tau}) = \begin{cases} d_{p2v} & , \frac{f({}^I\mathbf{f}|{}^I\mathbf{m})}{\bar{f}({}^I\mathbf{f}|{}^I\mathbf{m})} \geq c \\ K_m n_m & , otherwise \end{cases} \tag{15}$$

where n_m is the number of incorrect matchings, and K_m is the weighted value that trade-off the importance of the likelihood of correct matchings and the number of incorrect matchings. The LiDAR matching cost $\mathbf{r}_L(\mathbf{x}, \boldsymbol{\tau})$ defined in (15) can be expressed as a function of $\mathbf{x}$ and $\boldsymbol{\tau}$ due to the ${}^I\mathbf{f}_i$ in the likelihood function $L({}^I\mathbf{f}_i|{}^I\mathbf{m}_j)$ can be expressed as ${}^I\mathbf{f}_i = \mathbf{R}^B\mathbf{f}_i + \mathbf{t}$, where $\mathbf{R}_{t_k}$ and $\mathbf{t}_{t_k}$ are a part of state vector $\mathbf{x}_{t_k}$. The state vector $\mathbf{x}_{t_k}$ can be expressed as a function of $\mathbf{x}_{t_{k-1}}$ and $\mathbf{u}_{t_{k-1}}$ through the kinematic model (5), and $\mathbf{u}_{t_{k-1}}$ is the mean vector of $\boldsymbol{\tau}_{t_{k-1}}$.

The point-to-voxel distance d_{p2v} in (15) can be split into following two cases.

1) For edge features, the point-to-voxel distance between edge feature and edge voxel is defined as

$$d_{p2v}^{e} = \sum_{i=1}^{n_c^e} ({}^I\mathbf{f}_i^e - \mathbf{m}_j^{\mu_e})^\top (\mathbf{I} - \mathbf{m}_j^{n_e} \mathbf{m}_j^{n_e\top})({}^I\mathbf{f}_i^e - \mathbf{m}_j^{\mu_e}) \tag{16}$$

where n_c^e is the number of correct edge point-to-voxel matchings.

2) For planar features, the point-to-voxel distance between planar feature and planar voxel is defined as

$$d_{p2v}^{p} = \sum_{i=1}^{n_c^p} ({}^I\mathbf{f}_i^p - \mathbf{m}_j^{\mu_p})^\top \mathbf{m}_j^{n_p} \mathbf{m}_j^{n_p\top} ({}^I\mathbf{f}_i^p - \mathbf{m}_j^{\mu_p}) \tag{17}$$

where n_c^p is the number of correct planer point-to-voxel matchings.

Remark 1: Different from traditional LiDAR-based localization and mapping systems [11], [14], [18], the proposed LiDAR matching cost (15) considers the likelihood of correct matchings and the number of incorrect matchings simultaneously. For the novel LiDAR matching cost defined in (15), it penalizes states that produce incorrect matchings which could otherwise help improve the quality of localization and mapping.

B. Gradient-Free Optimization

Based on the above derivation, the problem solved in the present work can be summarized as

$$\hat{\mathbf{u}} = \arg\min_{\mathbf{u}} \mathbb{E}_{\mathcal{Q}}\left[\mathbf{r}_I(\mathbf{x}, \boldsymbol{\tau}) + \mathbf{r}_L(\mathbf{x}, \boldsymbol{\tau})\right]. \tag{18}$$

The cost function defined in (18), constitutes the IMU measurements residual $\mathbf{r}_I(\mathbf{x}, \boldsymbol{\tau})$ and the LiDAR matching residual $\mathbf{r}_L(\mathbf{x}, \boldsymbol{\tau})$, composed of (9)–(17). The stochastic optimization (18) is difficult to solve using traditional gradient-based methods, due to the nonlinear and noncontinuous LiDAR matching residual, which considers the likelihood of correct LiDAR matchings and the number of incorrect LiDAR matchings in a piecewise function formulation. In this article, a sampling-based and gradient-free optimization is adopted to solve the stochastic optimization problem (18), which is fully parallel and suitable for performing on GPU.

Assume that $\mathcal{Q}^*$ is the optimal distribution of $\boldsymbol{\tau}$, which makes $\mathbb{E}_{\mathcal{Q}^*}[\mathbf{S}(\mathbf{x}, \boldsymbol{\tau})]$ provides the lower bound of $\mathbb{E}_{\mathcal{Q}}[\mathbf{S}(\mathbf{x}, \boldsymbol{\tau})]$

$$\mathbb{E}_{\mathcal{Q}^*}\left[\mathbf{S}(\mathbf{x}, \boldsymbol{\tau})\right] \leq \mathbb{E}_{\mathcal{Q}}\left[\mathbf{S}(\mathbf{x}, \boldsymbol{\tau})\right]. \tag{19}$$

Hence, the stochastic optimization problem (18) can be converted into

$$\hat{\mathbf{u}} = \arg\min_{\mathbf{u}} \mathbb{E}_{\mathcal{Q}}\left[\mathbf{S}(\mathbf{x}, \boldsymbol{\tau})\right] \tag{20}$$

$$\triangleq \mathbb{E}_{\mathcal{Q}^*}(\boldsymbol{\tau}) = \int q^*(\mathbf{u})\mathbf{u}d\mathbf{u} \tag{21}$$

where q^* is the density function correspondence to the optimal distribution $\mathcal{Q}^*$. The step from (20) to (21) follows because $\mathbb{E}_{\mathcal{Q}}[\mathbf{S}(\mathbf{x}, \boldsymbol{\tau})]$ achieves the lower bound by sampling from the optimal distribution $\mathcal{Q}^*$. Hence, if the optimal distribution $\mathcal{Q}^*$ can be defined, the stochastic optimization problem (18) can be solved through calculate the expected value of $\boldsymbol{\tau}$ sampled from the optimal distribution $\mathcal{Q}^*$.

1) Optimal Distribution: The definition of the optimal density function q^* is crucial to solving (21), which can be derived from the lower bound of $\mathbb{E}_{\mathcal{Q}^*}[\mathbf{S}(\mathbf{x}, \boldsymbol{\tau})]$. As noted in [24], the lower bound of $\mathbb{E}_{\mathcal{Q}^*}[\mathbf{S}(\mathbf{x}, \boldsymbol{\tau})]$ can be defined as follows:

$$\begin{aligned}&\mathbb{E}_{\mathcal{Q}^*}\left(\mathbf{S}\left(\mathbf{x}, \boldsymbol{\tau}\right)\right) \geq \\ &-\lambda \log\left(\mathbb{E}_{\mathcal{Q}}\left[\exp\left(-\frac{1}{\lambda}\mathbf{S}\left(\mathbf{x}, \boldsymbol{\tau}\right)\right)\right]\right) - \lambda\mathbb{D}(\mathcal{Q}^*||\mathcal{Q})\end{aligned} \tag{22}$$

which establishes a relationship between the lower bound of $\mathbb{E}_{\mathcal{Q}^*}[\mathbf{S}(\mathbf{x}, \boldsymbol{\tau})]$ and the distribution $\mathcal{Q}$, $\lambda \in \mathbb{R}^+$ is a value similar to the kernel bandwidth of the Gaussian kernel function [25], and $\mathbb{D}(\mathcal{Q}^*||\mathcal{Q})$ is the KL-divergence between distributions $\mathcal{Q}^*$ and $\mathcal{Q}$, which can be expanded as follows:

$$\mathbb{D}(\mathcal{Q}^*||\mathcal{Q}) = \mathbb{E}_{\mathcal{Q}^*}\left[\log\left(\frac{q^*}{q}\right)\right] \tag{23}$$

where q^* and q are density functions correspondence to distributions $\mathcal{Q}^*$ and $\mathcal{Q}$, respectively.

Substituting (23) into (22) yields

$$\begin{aligned}&\lambda\mathbb{E}_{\mathcal{Q}^*}\left[\log\left(\frac{q^*}{q}\right)\right] \geq \\ &-\lambda \log\left(\mathbb{E}_{\mathcal{Q}}\left[\exp\left(-\frac{1}{\lambda}\mathbf{S}\left(\mathbf{x}, \boldsymbol{\tau}\right)\right)\right]\right) - \mathbb{E}_{\mathcal{Q}^*}\left[\mathbf{S}\left(\mathbf{x}, \boldsymbol{\tau}\right)\right]\end{aligned} \tag{24}$$

which leads to

$$\begin{aligned}&\lambda\mathbb{E}_{\mathcal{Q}^*}\left[\log\left(q^*\right)\right] - \lambda\mathbb{E}_{\mathcal{Q}^*}\left[\log(q)\right] \geq \\ &-\lambda \log\left(\mathbb{E}_{\mathcal{Q}}\left[\exp\left(-\frac{1}{\lambda}\mathbf{S}\left(\mathbf{x}, \boldsymbol{\tau}\right)\right)\right]\right) - \mathbb{E}_{\mathcal{Q}^*}\left[\mathbf{S}\left(\mathbf{x}, \boldsymbol{\tau}\right)\right].\end{aligned} \tag{25}$$

With the aim of finding the optimal density function q^*, (25) can be rewritten as follows:

$$\begin{aligned}\mathbb{E}_{\mathcal{Q}^*}\left[\log\left(q^*\right)\right] \geq \mathbb{E}_{\mathcal{Q}^*}&\left[-\log\left(\mathbb{E}_{\mathcal{Q}}\left[\exp\left(-\frac{1}{\lambda}\mathbf{S}\left(\mathbf{x}, \boldsymbol{\tau}\right)\right)\right]\right)\right] \\ &+\mathbb{E}_{\mathcal{Q}^*}\left[\log\left(\exp\left(-\frac{1}{\lambda}\mathbf{S}\left(\mathbf{x}, \boldsymbol{\tau}\right)\right)\right) + \log(q)\right]\end{aligned} \tag{26}$$

which can be simplified as

$$\mathbb{E}_{\mathcal{Q}^*}\left[\log\left(q^*\right)\right] \geq \mathbb{E}_{\mathcal{Q}^*}\left[\log\left(\frac{\exp\left(-\frac{1}{\lambda}\mathbf{S}\left(\mathbf{x}, \boldsymbol{\tau}\right)\right)q}{\mathbb{E}_{\mathcal{Q}}\left[\exp\left(-\frac{1}{\lambda}\mathbf{S}\left(\mathbf{x}, \boldsymbol{\tau}\right)\right)\right]}\right)\right]. \tag{27}$$

Hence, the optimal density function q^* can be defined as

$$q^* = \frac{\exp\left(-\frac{1}{\lambda}\mathbf{S}\left(\mathbf{x}, \boldsymbol{\tau}\right)\right)q}{\mathbb{E}_{\mathcal{Q}}\left(\exp\left(-\frac{1}{\lambda}\mathbf{S}\left(\mathbf{x}, \boldsymbol{\tau}\right)\right)\right)}. \tag{28}$$

According to the derivation in (23)–(27), the optimal density function defined in (28) can make $\mathbb{E}_{\mathcal{Q}^*}[\mathbf{S}(\mathbf{x}, \boldsymbol{\tau})]$ achieve the lower bound in (22), which means that the stochastic optimization problem (18) can be solved by substituting (28) into (21).

2) Importance Sampling: With the definition of the optimal distribution, (21) can be solved through the importance sampling technique [26], which compute expectations with respect to $\mathcal{Q}^*$ by sampling from $\mathcal{Q}$

$$\hat{\mathbf{u}} = \int \underbrace{\frac{q^*(\boldsymbol{\tau})}{q(\boldsymbol{\tau})}}_{w(\boldsymbol{\tau})} q(\boldsymbol{\tau})\boldsymbol{\tau}d\boldsymbol{\tau} = \mathbb{E}_{\mathcal{Q}}\left[w(\boldsymbol{\tau})\boldsymbol{\tau}\right] \tag{29}$$

where $w(\boldsymbol{\tau})$ is the weight of importance sampling.

In practice, the expectation $\mathbb{E}_{\mathcal{Q}}[w(\boldsymbol{\tau})\boldsymbol{\tau}]$ is difficult to perfectly evaluate. The optimal solution defined in (29) is approximated through a Monte-Carlo sampling

$$\hat{\mathbf{u}} = \sum_{i=0}^{m-1} \frac{\exp\left(-\frac{1}{\lambda}\mathbf{S}\left(\mathbf{x}, \mathbf{u}_i\right)\right)\mathbf{u}_i}{\sum_{j=0}^{m-1}\exp\left(-\frac{1}{\lambda}\mathbf{S}\left(\mathbf{x}, \mathbf{u}_j\right)\right)} \tag{30}$$

where m is the number of Monte-Carlo sampling, and $\mathbf{u}_i$ is a vector obtained from ith sampling on the Gaussian distribution $\mathcal{Q}(\mathbf{u}, \boldsymbol{\sigma}_u)$. The mean vector $\mathbf{u}$ is calculated by substituting raw IMU measurements into (8), and the covariance $\boldsymbol{\sigma}_u$ is a predefined matrix based on the IMU measurement noise. $\hat{\mathbf{u}}$ is the estimated vector of the angular velocity $\boldsymbol{\omega}$ and local linear acceleration $\mathbf{a}$. The state vector can be estimated by substituting

Algorithm 1: Gradient-free LiDAR-inertial odometry.

```
Input  : ${}^B\mathbf{F}$: Newly obtained feature set, ${}^I\mathbf{M}$: The voxel
         map, $m$: Number of samples, $\mathbf{u}_0$: The initial guess
         of $\mathbf{u}$.
Output: $\hat{\mathbf{x}}$: The estimated state vector.
for $i \leftarrow 0$ to $m-1$ do
    $\mathbf{u}_i \leftarrow SampleQ(\mathbf{u}_0, \boldsymbol{\sigma}_u)$;
    Get $\mathbf{T}_i$ from kinematic model (5) and $\mathbf{u}_i$;
    Compute the IMU measurment residual $\mathbf{r}_I(\mathbf{x}, \mathbf{u}_i)$;
    for each ${}^B\mathbf{f}_j \in {}^B\mathbf{F}$ do
        Transform ${}^B\mathbf{f}_j$ into the inertial frame ${}^I\mathbf{f}_j = \mathbf{T}_i^B\mathbf{f}_j$
        Find ${}^I\mathbf{m}_k = \mathrm{FMM}({}^I\mathbf{f}_j, {}^I\mathbf{M})$;
        if $IsCorrectMatching({}^I\mathbf{f}_j, {}^I\mathbf{m}_k)$ is true then
            if $\mathbf{f}_j \in \mathbf{F}^e$ then
                $\mathbf{r}_L(\mathbf{x}, \mathbf{u}_i) = \mathbf{r}_L(\mathbf{x}, \mathbf{u}_i) +$
                $({}^I\mathbf{f}_j - \mathbf{m}_k^{\mu_e})^\top (\mathbf{I} - \mathbf{m}_k^{n_e} \mathbf{m}_k^{n_e\top})({}^I\mathbf{f}_j - \mathbf{m}_k^{\mu_e})$
            else if $\mathbf{f}_j \in \mathbf{F}^p$ then
                $\mathbf{r}_L(\mathbf{x}, \mathbf{u}_i) = \mathbf{r}_L(\mathbf{x}, \mathbf{u}_i) +$
                $({}^I\mathbf{f}_j - \mathbf{m}_k^{\mu_p})^\top \mathbf{m}_k^{n_p} \mathbf{m}_k^{n_p\top} ({}^I\mathbf{f}_j - \mathbf{m}_k^{\mu_p})$
        else
            $\mathbf{r}_L(\mathbf{x}, \mathbf{u}_i) = \mathbf{r}_L(\mathbf{x}, \mathbf{u}_i) + K_m$
    $\mathbf{S}(\mathbf{x}, \mathbf{u}_i) = \mathbf{r}_I(\mathbf{x}, \mathbf{u}_i) + \mathbf{r}_L(\mathbf{x}, \mathbf{u}_i)$
$\hat{\mathbf{u}} = \sum_{i=0}^{m-1} \frac{\exp\left(-\frac{1}{\lambda}\mathbf{S}(\mathbf{x},\mathbf{u}_i)\right)\mathbf{u}_i}{\sum_{j=0}^{m-1} \exp\left(-\frac{1}{\lambda}\mathbf{S}(\mathbf{x},\mathbf{u}_j)\right)}$
Get $\hat{\mathbf{x}}$ from kinematic model (5) and $\hat{\mathbf{u}}$;
return $\hat{\mathbf{x}}$
```

(30) into the kinematic model defined in (5). The process of the proposed gradient-free LiDAR-inertial odometry is given in Algorithm 1.

Remark 2: Different from traditional LiDAR-based localization and mapping systems [11], [14], [18], the LiDAR-inertial odometry described in Algorithm 1 is fully paralleled, which can be performed efficiently with a GPU. In [11], [14], [18], the localization and mapping problem is solved through gradient optimization or IEKF, which is time-consuming due to the LiDAR matching process for each iteration. For the proposed method, a Monte-Carlo sampling is adopted to solve the optimization with a single parallel iteration, which significantly improves the real-time performance of the LiDAR-inertial odometry. Moreover, the computation of Jacobians can be problematic for complex systems, the gradient-free optimization introduced in this article does not require to deriving the Jacobians, which makes the algorithm flexible to deal with noncontinuous constraints.

C. Practical Implementation

The proposed LiDAR-inertial odometry build with the Robots Operating System (ROS) under Ubuntu. The feature extraction and voxel mapping process are implemented on the CPU, and the gradient-free optimization process described in Algorithm 1 is implemented on a GPU with Nvidia's CUDA architecture. It is worth noting that, there exists a nested loop in Algorithm 1. In order to deploy Algorithm 1 on GPU parallelly, a dynamic-parallelism-like strategy [27] is adopted. In our implementation, Algorithm 1 uses $m \times k$ CUDA threads, where m is the number of Monte-Carlo sampling and k is the number of features. For example, the lth CUDA thread, where $0 \leq l < m \times k$, is in charge of calculating LiDAR measurements residual corresponding to $\mathrm{mod}(l, k)$th feature and l/kth Monte-Carlo sampling. All the residuals calculated in 0 to $m \times k - 1$ CUDA threads are saved in a matrix with a dimension of $m \times k$. The cost function $\mathbf{S}(\mathbf{x}, \mathbf{u}_i)$, $i = 0, \ldots, m-1$, is calculated by summing all the column vectors of the matrix through a reduction sum operation in CUDA Thrust [28].

Predefined parameters of Algorithm 1 are set to $c = 0.98$, and $\boldsymbol{\sigma}_u = \mathrm{diag}(3.0, 3.0, 3.0, 0.1, 0.1, 0.1)$ for all experiments evaluated in Section V. As noted in [24], the negative exponentiation required by (30) is numerically sensitive to the range of the input values. For this reason, we shift the range of the costs $\mathbf{S}$ so that the best cost sampled has a value of 0. Define $\mathbf{S}_{\text{min}}$ as the minimum cost of $\mathbf{S}(\mathbf{x}, \mathbf{u}_i), i = 0, \ldots, m-1$, where m is the number of Monte-Carlo sampling. Multiply $\exp(\frac{1}{\lambda}\mathbf{S}_{\text{min}})/\exp(\frac{1}{\lambda}\mathbf{S}_{\text{min}})$ to (30) results in

$$\hat{\mathbf{u}} = \sum_{i=0}^{m-1} \frac{\exp\left(-\frac{1}{\lambda}\left(\mathbf{S}\left(\mathbf{x}, \mathbf{u}_i\right) - \mathbf{S}_{\text{min}}\right)\right)\mathbf{u}_i}{\sum_{j=0}^{m-1} \exp\left(-\frac{1}{\lambda}\left(\mathbf{S}\left(\mathbf{x}, \mathbf{u}_j\right) - \mathbf{S}_{\text{min}}\right)\right)} \tag{31}$$

which can prevent numerical overflow or underflow. The $\exp(-\frac{1}{\lambda}(\mathbf{S}(\mathbf{x}, \mathbf{u}_i) - \mathbf{S}_{\text{min}}))$ in (31) is similar to the Gaussian kernel function formulation [25], where the parameter λ is corresponding to the kernel bandwidth. As noted in [25], the spatial extent of the Gaussian kernel ranges from $-\infty$ to $+\infty$, but in practice, it has negligible values for $(\mathbf{S}(\mathbf{x}, \mathbf{u}_i) - \mathbf{S}_{\text{min}})$ larger than a few (say 5) λ. Hence, if $\lambda \ll (\mathbf{S}(\mathbf{x}, \mathbf{u}_i) - \mathbf{S}_{\text{min}})$ the solution of (31) places all its mass on a single Monte-Carlo sampling, whereas as $\lambda \gg (\mathbf{S}(\mathbf{x}, \mathbf{u}_i) - \mathbf{S}_{\text{min}})$ all the Monte-Carlo sampling have close equal weight. To prevent the numerical instability of (31), the parameter λ is set as a self-adapting value according to the average cost $\mathbf{S}_{\text{mean}}$ and the minimum cost $\mathbf{S}_{\text{min}}$. We set $\lambda = (\mathbf{S}_{\text{mean}} - \mathbf{S}_{\text{min}})/5$ for all experiments evaluated in Section V.

V. Results

In this section, the effectiveness of the proposed LiDAR-inertial odometry is demonstrated through various scenarios, including public datasets and real-world experiments. For more details, a video demonstration is available online.[1]

A. Quantitative Evaluation on the NTU VIRAL Datasets

The proposed LiDAR-inertial odometry is evaluated quantitatively on the NTU VIRAL dataset [29], which provides point clouds captured by two 16-channel lightweight LiDAR OS1 (horizontal LiDAR measurements are used in experiments), high-frequency inertial data, and ground truth from the Leica laser tracker. Different from datasets with 3D LiDAR mounted on ground vehicles, the NTU VIRAL dataset is aerial vehicle viewpoint, which has much more complex motion in 3D space with frequent aggressive rotational and translational motions.

[1] [Online].Available: https://b23.tv/1bMhFY5

TABLE I
ABSOLUTE TRAJECTORY ERROR (ATE, METERS) OVER NTU VIRAL DATASETS

Method	Proposed 512			Proposed 1024			Proposed 2048			FAST-LIO2	LIO-SAM	LOAM
	$K_m = 0$	$K_m = 0.5$	$K_m = 1.0$	$K_m = 0$	$K_m = 0.5$	$K_m = 1.0$	$K_m = 0$	$K_m = 0.5$	$K_m = 1.0$			
eee 01	-[1]	0.1429	0.1379	-	0.0996	**0.0949**	-	**0.0944**	**0.0955**	0.2096	0.1022	0.2309
eee 02	-	0.1192	0.1610	-	0.0865	**0.0830**	-	**0.0840**	**0.0796**	0.1649	0.1113	0.1963
eee 03	-	0.1415	0.1613	-	0.1132	**0.1089**	-	**0.1067**	**0.1108**	0.1945	0.1469	0.1730
nya 01	-	0.1277	0.1245	-	**0.0962**	0.1030	-	**0.0937**	0.0977	0.1217	**0.0943**	0.0973
nya 02	-	0.1425	0.1406	-	**0.1138**	0.1233	-	**0.1071**	0.1212	0.2424	0.1200	**0.1165**
nya 03	-	0.1239	0.1230	-	0.1098	0.1062	-	**0.1025**	0.1064	0.1349	**0.1049**	**0.1029**
sbs 01	-	0.1242	0.1237	-	0.1044	**0.0998**	-	**0.0964**	**0.0965**	0.1600	0.1072	0.1793
sbs 02	-	0.1270	0.1264	-	0.1075	0.1006	-	**0.0977**	**0.0968**	0.1831	**0.0980**	0.1175
sbs 03	-	0.1157	0.1167	-	0.0968	**0.0962**	-	**0.0903**	**0.0953**	0.1519	0.1034	0.3016

[1] - denotes that the system failure.

The best result is highlighted in Blue, the second best result is highlighted in Red, and the third best result is highlighted in bold.

We compare our work with current state-of-the-art LiDAR-based odometry such as LOAM[2] [11], LIO-SAM[3] [14], and FAST-LIO2[4] [18]. For a fair comparison, all methods are implemented without loop closure. Moreover, an ablation study on the proposed method is performed to understand the influence of the sampling number, we run the algorithm in various Monte-Carlo sampling numbers of 512, 1024, 2048, so-called proposed 512, proposed 1024, proposed 2048, respectively. Each experiment is conducted on a computer equipped with an Intel Core i7-7700 and an NVIDIA GeForce GTX 1080.

1) Accuracy Evaluation: To quantitatively evaluate the accuracy of the LiDAR-inertial odometry, the absolute trajectory error (ATE) results of each method over NTU VIRAL datasets are shown in Table I. An ablation study on the parameter K_m is also performed to understand the effect of incorrect LiDAR matchings considered in (15). For $K_m = 0$, which means only correct LiDAR matchings are considered in the LiDAR matching cost, the proposed method converges into a suboptimal local minimum that leads to system failure. As an extreme example, assuming that there exists a transformation $\hat{\mathbf{T}}$ that matches all the features to the incorrect voxels. Obviously, the transformation $\hat{\mathbf{T}}$ is a suboptimal local minimum when $K_m = 0$. For $K_m > 0$, the novel LiDAR matching cost defined in (15) penalizes states that produce incorrect matchings, which could otherwise help improve the quality of localization and mapping and attempts to escape the local minimum. From the results shown in Table I, for $K_m > 0$, better accuracy can be achieved when a higher number of samples is adopted for the proposed method, and the proposed method with 2048 samples achieves the best accuracy in all data sequences. This is because the gradient-free optimization algorithm introduced in Section IV-B is a suboptimal estimator, which approximates the optimal solution through the Monte-Carlo sampling, and the approximation performance is determined by the number of samples. In Table I, we also compare the ATE of the proposed method at $K_m = 0.5$ and $K_m = 1.0$. In all sequences, the accuracy of the proposed method with $K_m = 0.5$ performs similarly to $K_m = 1.0$, and we choose $K_m = 0.5$ for all the rest of the experiments performed in this section. The comparison between the proposed method with 2048 samples and ground truth is shown in Fig. 2(a).

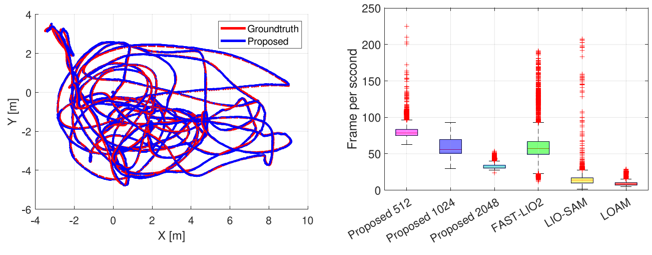

(a) (b)

Fig. 2. Comparison results of under the nya 03 sequence. (a) Trajectories. (b) Frames pre second (FPS).

2) Running Time Evaluation: Table II shows the average running time for process one scan of the proposed method with different sampling numbers, and each state-of-the-art method. The time consumption of each individual component, including feature extraction ("FE" in Table II), state estimation ("SE" in Table II), and mapping ("Map" in Table II), are compared across all 9 sequences. For the feature extraction, FAST-LIO2 achieves the best real-time performance, due to FAST-LIO2 registering raw points to the map without extracting features. Thanks to the fully paralleled optimization algorithm introduced in Section IV-B, which can be accelerated through massive parallel sampling on a GPU, the proposed method with 512 samples achieves the best real-time performance in state estimation, and the proposed method with 1024 samples (state estimated by the scan-to-map matching) achieves a similar state estimation time with LOAM (state estimated by the scan-to-scan matching). For the mapping time, the proposed method maintains a voxel map in a hash table instead of a KD-tree used in LIO-SAM and LOAM or the iKD-tree used in FAST-LIO2. It is worth noting that, similar to FAST-LIO2, the proposed method maintains the voxel map incrementally without re-build the local map in KD-Tree (the time complexity of re-building the KD-Tree is $O(n \log n)$ [17]). Furthermore, thanks to the effective data insertion operation of hash data structure, which takes a constant time complexity of $O(1)$, features can insert into the voxel map more efficiently, when compared with the iKD-tree adopted in FAST-LIO2 (the time complexity of point insertion on iKD-tree is $O(\log n)$ [18]). The total time for feature extraction, state estimation,

[2] [Online].Available: https://github.com/brytsknguyen/A-LOAM
[3] [Online].Available: https://github.com/brytsknguyen/LIO-SAM
[4] [Online].Available: https://github.com/shenhm0516/FAST_LIO

TABLE II
AVERAGE PROCESSING TIME (MILLISECONDS) FOR INDIVIDUAL COMPONENTS WHEN PROCESSING ONE SCAN

Method	Proposed 512				Proposed 1024				Proposed 2048				FAST-LIO2				LIO-SAM				LOAM			
	Total	FE	SE	Map	Total	FE	SE	Map	Total	FE	SE	Map	Total	FE	SE	Map	Total	FE	SE	Map	Total	FE	SE	Map
eee 01	**15.60**	**2.17**	**11.70**	**1.72**	**25.30**	**2.18**	21.66	**1.46**	40.15	2.33	36.07	**1.76**	**22.23**	**0**	**18.16**	4.07	125.47	2.29	42.99	80.19	229.28	3.04	**15.26**	210.98
eee 02	**15.89**	3.22	**10.96**	**1.72**	**23.26**	**2.31**	**19.42**	**1.53**	38.08	**2.54**	33.76	**1.78**	**27.94**	**0**	23.26	4.68	102.69	2.96	40.79	58.95	193.61	3.30	**14.93**	175.37
eee 03	**16.36**	**3.18**	**11.31**	**1.87**	**25.59**	3.32	**20.70**	**1.57**	**39.74**	3.42	34.50	**1.82**	40.38	**0**	32.23	8.14	112.00	**2.76**	50.01	59.23	173.55	3.23	**15.19**	155.13
nya 01	**12.26**	**3.06**	**8.08**	**1.12**	**18.05**	3.34	**13.48**	**1.24**	30.56	3.30	25.60	**1.66**	**26.86**	**0**	23.63	3.23	75.61	**3.22**	28.81	43.58	126.81	3.23	**15.15**	108.43
nya 02	**12.19**	**3.12**	**7.92**	**1.15**	**18.15**	3.59	**13.24**	**1.52**	30.06	3.33	25.04	**1.69**	**25.34**	**0**	22.78	2.56	78.47	**3.07**	37.01	38.38	132.27	3.17	**15.24**	113.85
nya 03	**12.74**	**3.19**	**8.01**	**1.15**	**17.28**	3.21	**12.79**	**1.27**	30.56	3.37	25.49	**1.69**	**18.85**	**0**	16.97	1.88	80.16	**3.13**	30.95	46.08	136.76	3.34	**15.94**	117.48
sbs 01	**13.27**	**2.41**	**9.36**	**1.50**	**21.50**	2.84	**17.15**	**1.51**	33.46	**2.39**	29.29	**1.78**	**28.64**	**0**	24.41	4.23	102.98	2.56	41.10	59.23	192.29	**2.56**	**12.94**	176.78
sbs 02	**13.22**	**2.48**	**9.28**	**1.47**	**20.50**	2.88	**16.09**	**1.53**	33.17	2.60	28.76	**1.81**	**20.89**	**0**	17.89	3.01	99.62	2.67	34.81	62.19	193.54	2.61	**12.89**	178.04
sbs 03	**13.07**	**2.49**	**9.12**	**1.47**	**21.06**	2.98	**16.58**	**1.50**	33.56	2.49	29.28	**1.80**	**32.15**	**0**	27.74	4.40	96.41	2.62	33.30	60.48	208.85	**2.43**	**13.02**	193.40

The best result is highlighted in Blue, the second best result is highlighted in Red, and the third best result is highlighted in bold.

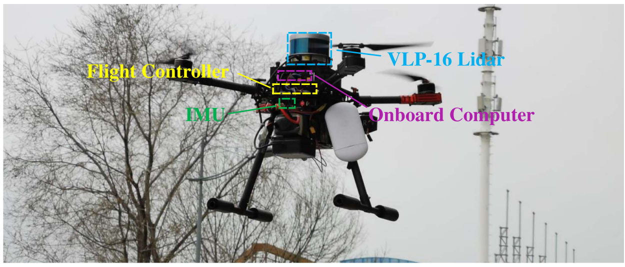

Fig. 3. Aerial platform used in real-world experiments.

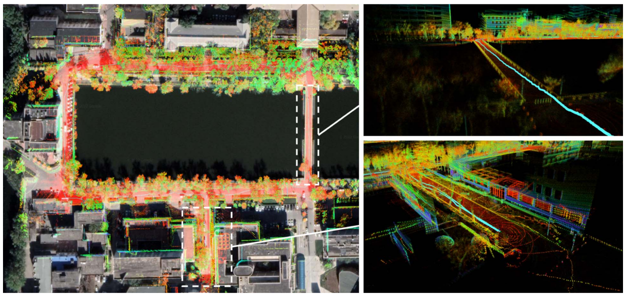

Fig. 4. Mapping result of the proposed method.

and mapping ultimately affects the real-time performance of the localization and mapping system, which is also summarized in Table II ("Total" in Table II). As the results show in Tables I and II, for the proposed method, the number of samples is a tradeoff between accuracy and real-time performance. The proposed method with 2048 samples outperforms each state-of-the-art method in accuracy with an acceptable processing time. Compared with optimization-based methods, LOAM and LIO-SAM, the proposed method with 1024 samples achieves a comparative accuracy and a significant efficiency improvement, which saves 70%–90% processing time, and the proposed method with 512 samples achieves the best real-time performance in all data sequences. Fig. 2(b) shows the frames per second (FPS) on nya 03 sequence. The result indicated that the proposed LiDAR-inertial odometry reaches the speed of over 200 Hz and achieves 1.5–2 times FPS compared with FAST-LIO2.

B. Real-World Experiments

To attest the practicality of the proposed localization and mapping method, a variety of real-world experiments is performed with a quadrotor aerial platform. As shown in Fig. 3, the aerial platform is equipped with a Pixhawk4 flight controller, a Velodyne VLP-16 LiDAR, a MicroStrain 3DM-GX5-25 IMU, and a low-power onboard computer (Nvidia Xavier worked with the 30 W 6 Core power model). The real-world experiments are divided into two parts: 1) Verification of real-time performance and global consistency in a large-scale urban environment. 2) Autonomous flight in a GPS-denied environment.

1) High Precision Map Building in Real-Time: To evaluate the performance of the proposed LiDAR-inertial odometry, a MAV running the proposed method with 512 samples onboard is flown manually to reconstruct a dense 3-D, high-precision, large-scale map of campus in real-time. The mapping result is shown in Fig. 4, which is merged with the Google Earth image to examine the accuracy of the proposed method. This experiment is convincing due to the fact that MAV has to travel through a bridge over an open lake, typically a challenging scene for the LiDAR-based localization and mapping system, and the result shows that the proposed method can close the loop when MAV returns to the start point without loop closure. The high-quality point cloud demonstrates that the proposed LiDAR-inertial odometry is able to provide high-precision reconstruction in a large-scale environment. To analyze the accuracy and real-time performance of the proposed method, we compare the proposed method with FAST-LIO2 [18], LIO-SAM [14], LOAM [11], CLINS [15], and LINS [13] on a low-power ARM onboard computer (Nvidia Xavier). From the result shown in Table III, thanks to the parallel acceleration of the low-power onboard GPU, the proposed method achieves the best real-time performance than other methods. Compared with optimization-based methods, the proposed method is 8 times faster than LIO-SAM, 12 times faster than LOAM, and 15 times faster than CLINS. Even compared with the state-of-the-art filter-based method

TABLE III
END-TO-END ERROR (METERS) AND AVERAGE PROCESSING TIME (MILLISECONDS) FOR INDIVIDUAL COMPONENTS WHEN PROCESS ONE SCAN

Method	Proposed	FAST-LIO2	LIO-SAM	LOAM	CLINS	LINS
Feature Extraction	6.85	**0**	11.78	24.43	13.55	15.79
State Estimation	**40.47**	58.59	244.92	51.41	741.51	63.22
Mapping	**2.14**	6.54	141.44	528.85	21.20	269.17
Total	**49.46**	65.13	398.12	604.69	776.26	348.18
End-to-End Error	**0.12**	0.17	5.33	19.02	14.12	30.52

The best result is highlighted in BOLD.

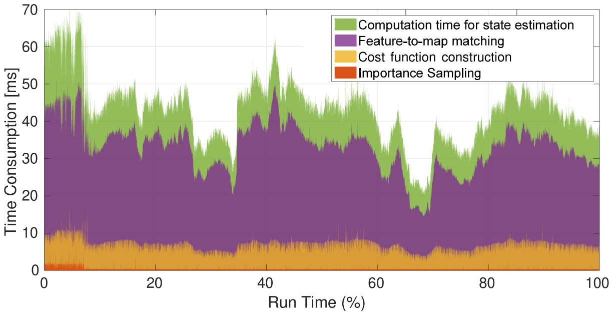

Fig. 5. Computation time for state estiamtion.

FAST-LIO2, the proposed method saves more than 24% of the total processing time and is 7 times faster than LINS. For accuracy, end-to-end errors are also reported in Table III. Both LIO-SAM, LOAM, CLINS, and LINS show large drift because their total computation time greatly exceeded 100 ms, which leads them to drop a lot of LiDAR scan to achieve real-time performance. When compared with FAST-LIO2, the state-of-the-art filter-based LiDAR odometry, the proposed method still shows better end-to-end accuracy and real-time performance, thanks to the fully paralleled optimization method introduced in Section IV-B. Fig. 5 reports the computation time for the individual components of state estimation (the method described in Algorithm 1) when performing the large-scale reconstruction. The FMM process dominates the real-time performance of the state estimation process, which is in charge of finding correspondence voxel for each feature. It should be noted that the FMM process can be quite computationally expensive since $512 \times k$ features should be conducted, where 512 is the number of Monte-Carlo sampling, and k is the number of features in one sampling. In this article, the FMM process is split into $512 \times k$ threads and accelerated through Nvidia CUDA. Thanks to this strategy, we can cut down the mean FMM time to 34.33 ms compared to several seconds when using a single CPU thread. While cost function construction process is accelerated through a reduction sum operation in CUDA Thrust [28] (details can be found in Section IV-C), has an average processing time of 5.72 ms, and the optimal solution is approximated through an importance sampling technique, which has an average processing time of 0.42 ms. Thank to the Gradient-free optimization method introduced in Section IV-B, which can approximate optimal solution with a single parallel-iteration solver, the proposed tightly coupled LiDAR odometry has highly real-time performance under low-power GPU acceleration. The average running time of the proposed method for process one scan is 49.46 ms, much less than 100 ms, which demonstrates that the proposed LiDAR-inertial odometry can achieve real-time without dropping any scan (LiDAR rotation rate is 10 Hz) and is suitable to perform on low-power onboard computing power.

2) Application of MAV Autonomous Flight: To attest the practicality of the proposed localization and mapping method, two autonomous flights are performed, which are called *aggressive flight test* and *fully autonomous flight test*. During the aggressive flight test, the proposed method is used for feedback control of the MAV, which tracks a high-speed trajectory. Poses estimated by the proposed method are shown in Fig. 6(a), in addition, the linear velocity and angular velocity are shown in Fig. 6(b). The maximum velocity reaches 9 m/s, the maximum angular velocity achieves 180 deg/s (the square root of the triaxial angular rate achieves 245 deg/s) during the aggressive flight test. The results show that the proposed LiDAR-inertial odometry is suitable for MAV real-time control and trajectory tracking. For the fully autonomous flight test, a real-world autonomous flight is performed in a cluttered forest scenario. This test is illustrated due to only the onboard computing power is adopted to run the proposed localization and mapping algorithm with the additional workload, such as the motion planning algorithm [30], sensor drivers, in real-time. During this flight test, MAV track the reference trajectories for achieving obstacles avoidance, and the localization and mapping results are illustrated in Fig. 7. The results demonstrated that the proposed LiDAR-inertial odometry has the ability to enable the fully autonomous flight without a prior map and external sensings.

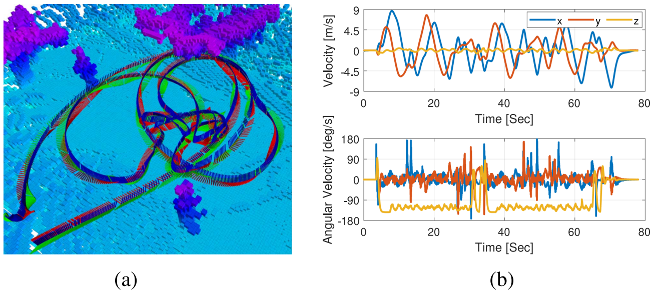

Fig. 6. Results of the aggresive flight test. (a) Estimated poses. (b) Velocity and anglular velocity.

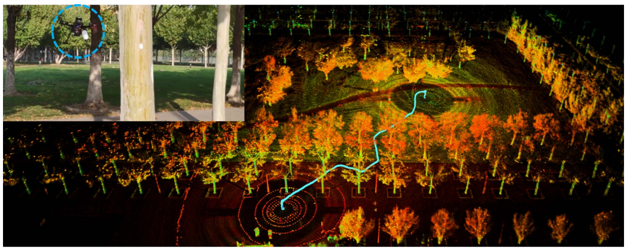

Fig. 7. Fully autonomous flight.

VI. Conclusion

In this article, an efficient and high-accuracy localization and mapping algorithm was developed for MAV. The proposed method formulated the localization and mapping problem as a stochastic optimization problem, which fuses IMU measurements and LiDAR measurements in a tightly coupled manner. A novel LiDAR matching cost was constructed by formulating the LiDAR matching problem as an MLE problem and simplifying it as a piecewise function through GMM and acceptance–rejection sampling, which consider the likelihood of correct matchings and the number of incorrect matchings simultaneously. Thanks to the gradient-free optimization, the nonlinear, and noncontinuous stochastic optimization problem is solved by a fully paralleled Monte-Carlo sampling, which can provide real-time localization and mapping with a low-power onboard computer. The proposed LiDAR-inertial odometry is validated with an extensive evaluation in both public datasets and real-world experiments. The results showed that the proposed method produces real-time and accurate localization and mapping results, and has a great potential to enable many autonomous aerial robots applications.

References

[1] L. Fusini, T. I. Fossen, and T. A. Johansen, "Nonlinear observers for GNSS- and camera-aided inertial navigation of a fixed-wing UAV," *IEEE Trans. Control Syst. Technol.*, vol. 26, no. 5, pp. 1884–1891, Sep. 2018, doi: 10.1109/TCST.2017.2735363.

[2] F. Nan, S. Sun, P. Foehn, and D. Scaramuzza, "Nonlinear MPC for quadrotor fault-tolerant control," *IEEE Robot. Automat. Lett.*, vol. 7, no. 2, pp. 5047–5054, Apr. 2022, doi: 10.1109/LRA.2022.3154033.

[3] T.-M. Nguyen, M. Cao, S. Yuan, Y. Lyu, T. H. Nguyen, and L. Xie, "VIRAL-fusion: A visual-inertial-ranging-LiDAR sensor fusion approach," *IEEE Trans. Robot.*, vol. 38, no. 2, pp. 958–977, Apr. 2022, doi: 10.1109/TRO.2021.3094157.

[4] K. Koide, J. Miura, and E. Menegatti, "A portable three-dimensional lidar-based system for long-term and wide-area people behavior measurement," *Int. J. Adv. Robot. Syst.*, vol. 16, no. 2, 2019, Art. no. 1729881419841532, doi: 10.1177/1729881419841532.

[5] S. Umeyama, "Least-squares estimation of transformation parameters between two point patterns," *IEEE Comput. Archit. Lett.*, vol. 13, no. 04, pp. 376–380, Apr. 1991.

[6] A. Segal, D. Haehnel, and S. Thrun, "Generalized-icp," in *Proc. Robot.: Sci. Syst.*, Seattle, USA, 2009, doi: 10.15607/RSS.2009.V.021.

[7] P. Biber and W. Straßer, "The normal distributions transform: A new approach to laser scan matching," in *Proc. IEEE/RSJ Int. Conf. Intell. Robots Syst.*, 2003, vol. 3, pp. 2743–2748.

[8] M. Yokozuka, K. Koide, S. Oishi, and A. Banno, "Litamin: LiDAR-based tracking and mapping by stabilized ICP for geometry approximation with normal distributions," in *Proc. IEEE/RSJ Int. Conf. Intell. Robots Syst.*, 2020, pp. 5143–5150, doi: 10.1109/IROS45743.2020.9341341.

[9] M. Yokozuka, K. Koide, S. Oishi, and A. Banno, "Litamin2: Ultra light LiDAR-based SLAM using geometric approximation applied with kl-divergence," in *Proc. IEEE Int. Conf. Robot. Automat.*, 2021, pp. 11619–11625, doi: 10.1109/ICRA48506.2021.9560947.

[10] K. Chen, B. T. Lopez, A.-A. Agha-mohammadi, and A. Mehta, "Direct LiDAR odometry: Fast localization with dense point clouds," *IEEE Robot. Automat. Lett.*, vol. 7, no. 2, pp. 2000–2007, Apr. 2022, doi: 10.1109/LRA.2022.3142739.

[11] J. Zhang and S. Singh, "Loam: Lidar odometry and mapping in real-time," in *Proc. Robot.: Sci. Syst.*, Berkeley, USA, 2014. [Online]. Available: http://www.roboticsproceedings.org/rss10/p07.html

[12] H. Ye, Y. Chen, and M. Liu, "Tightly coupled 3D LiDAR inertial odometry and mapping," in *Proc. IEEE Int. Conf. Robot. Automat.*, 2019, pp. 3144–3150.

[13] C. Qin, H. Ye, C. E. Pranata, J. Han, S. Zhang, and M. Liu, "Lins: A LiDAR-inertial state estimator for robust and efficient navigation," in *Proc. IEEE Int. Conf. Robot. Automat.*, 2020, pp. 8899–8906, doi: 10.1109/ICRA40945.2020.9197567.

[14] T. Shan, B. Englot, D. Meyers, W. Wang, C. Ratti, and D. Rus, "Lio-sam: Tightly-coupled LiDAR inertial odometry via smoothing and mapping," in *Proc. IEEE/RSJ Int. Conf. Intell. Robots Syst.*, 2020, pp. 5135–5142.

[15] J. Lv, K. Hu, J. Xu, Y. Liu, X. Ma, and X. Zuo, "Clins: Continuous-time trajectory estimation for LiDAR-inertial system," in *Proc. IEEE/RSJ Int. Conf. Intell. Robots Syst.*, 2021, pp. 6657–6663, doi: 10.1109/IROS51168.2021.9636676.

[16] W. Xu and F. Zhang, "Fast-lio: A fast, robust LiDAR-inertial odometry package by tightly-coupled iterated Kalman filter," *IEEE Robot. Automat. Lett.*, vol. 6, no. 2, pp. 3317–3324, Apr. 2021, doi: 10.1109/LRA.2021.3064227.

[17] Y. Cai, W. Xu, and F. Zhang, "ikd-Tree: An incremental kd tree for robotic applications," 2021, *arXiv:2102.10808*.

[18] W. Xu, Y. Cai, D. He, J. Lin, and F. Zhang, "Fast-lio2: Fast direct LiDAR-inertial odometry," *IEEE Trans. Robot.*, vol. 38, no. 4, pp. 2053–2073, Aug. 2022, doi: 10.1109/TRO.2022.3141876.

[19] Z. Liu and F. Zhang, "Balm: Bundle adjustment for LiDAR mapping," *IEEE Robot. Automat. Lett.*, vol. 6, no. 2, pp. 3184–3191, Apr. 2021.

[20] B. D. Flury, "Acceptance–rejection sampling made easy," *SIAM Rev.*, vol. 32, no. 3, pp. 474–476, 1990.

[21] H. Shen, Q. Zong, B. Tian, and H. Lu, "Voxel-based localization and mapping for multi-robot system in GPS-denied environments," *IEEE Trans. Ind. Electron.*, vol. 69, no. 10, pp. 10333–10342, Oct. 2022, doi: 10.1109/TIE.2022.3153822.

[22] C. Forster, L. Carlone, F. Dellaert, and D. Scaramuzza, "IMU preintegration on manifold for efficient visual-inertial maximum-a-posteriori estimation," in *Proc. Robot., Sci. Syst.*, Rome, Italy, 2015. [Online]. Available: http://www.roboticsproceedings.org/rss11/p06.html

[23] T. Stoyanov, M. Magnusson, H. Andreasson, and A. J. Lilienthal, "Fast and accurate scan registration through minimization of the distance between compact 3D NDT representations," *Int. J. Robot. Res.*, vol. 31, no. 12, pp. 1377–1393, 2012.

[24] G. Williams, P. Drews, B. Goldfain, J. M. Rehg, and E. A. Theodorou, "Information-theoretic model predictive control: Theory and applications to autonomous driving," *IEEE Trans. Robot.*, vol. 34, no. 6, pp. 1603–1622, Dec. 2018, doi: 10.1109/TRO.2018.2865891.

[25] B. M. ter Haar Romeny, "The Gaussian kernel," *Front-End Vision and Multi-Scale Image Analysis: Multi-Scale Computer Vision Theory and Applications, Written in Mathematics*. New York, NY, USA: Springer, 2003, pp. 37–51.

[26] A. Doucet et al., *Sequential Monte Carlo Methods in Practice*, vol. 1, no. 2. New York, NY, USA: Springer, 2001.

[27] S. Jones, "Introduction to dynamic parallelism," in *Proc. GPU Technol. Conf. Presentation S*, vol. 338, 2012, Art. no. 2012.

[28] N. Bell and J. Hoberock, "Thrust: A productivity-oriented library for cuda," in *Proc. GPU Comput. Gems Jade Ed.*, New York, NY, USA: Elsevier, 2012, pp. 359–371.

[29] T.-M. Nguyen, S. Yuan, M. Cao, Y. Lyu, T. H. Nguyen, and L. Xie, "NTU viral: A visual-inertial-ranging-lidar dataset, from an aerial vehicle viewpoint," *Int. J. Robot. Res.*, vol. 41, no. 3, pp. 270–280, 2022, doi: 10.1177/02783649211052312.

[30] H. Lu, Q. Zong, S. Lai, B. Tian, and L. Xie, "Real-time perception-limited motion planning using sampling-based MPC," *IEEE Trans. Ind. Electron.*, vol. 69, no. 12, pp. 13182–13191, Dec. 2022, doi: 10.1109/TIE.2022.3140533.

Hongming Shen received the B.S. degree in flight vehicle design and engineering from Central North University, Taiyuan, China, in 2015, and the M.S. degree in aerospace transportation and control from Beijing Institute of Technology, Beijing, China, in 2017. He is currently working toward the Ph.D. degree in control theory and control engineering with Tianjin University, Tianjin, China.

His current research interests include state estimation, multisensor fusion, localization and mapping, and aerial Robotics.

Qun Zong received the B.S., M.S., and Ph.D. degrees in automatic control from Tianjin University, Tianjin, China, in 1983, 1988, and 2002, respectively.

He is currently a Professor and one of the academic pacesetters in control theory and control engineering with the School of Electrical and Information Engineering, Tianjin University. He is also the Director of the New Aircraft Guidance and Control Center of the Ministry of Education, the Expert Groups Deputy Head of the Major Project of the Chinese Ministry of Education, Beijing, China, and the Deputy Director of the New Aircraft Joint Research Center, Tianjin. His current research interests include guidance, control and simulation for flight vehicles, coordination control of multiagent systems, fault diagnosis and fault-tolerant control, and optimization control.

Dr. Zong is also a Committee Member of the Chinese Association of the Automation Control Theory Technical Committee, the Guidance, Navigation and Control Technical Committee of Chinese Society of Aeronautics and Astronautics (CSAA), and so on. He also serves as an Editorial Board Member for several scientific journals, including *Journal of Control Theory and Applications* and *Journal of Astronautics*.

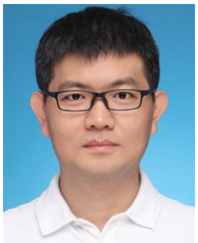

Bailing Tian received the B.S., M.S. and Ph.D degrees in automatic control from Tianjin University, Tianjin, China, in 2006, 2008, and 2011, respectively.

He was an Academic Visitor with the School of Electrical and Electronic Engineering, University of Manchester from June 2014 to June 2015. He is currently a Professor with the School of Electrical and Information Engineering, Tianjin University. His main research interests include finite time control, motion planning, simultaneous localization and mapping, and integrated guidance and control for unmanned systems.

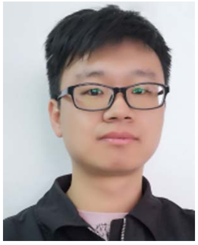

Xuewei Zhang received the B.S. degree in automatic control from Hebei University of Technology, Tianjin, China, in 2019. He is currently working toward the Ph.D. degree with the School of Electrical and Information Engineering, Tianjin University, Tianjin.

His research interests include motion planning of micro-aerial vehicles, simultaneous localization, and mapping.

Hanchen Lu received the B.S. degree in automatic control from Central South University, Changsha, China, in 2015. He is currently working toward the Ph.D. degree in motion planning with School of Electrical and Information Engineering, Tianjin University, Tianjin, China.

From September 2019 to September 2020, he was a Visiting Student with the School of Electrical and Electronic Engineering, Nanyang Technological University, Singapore. His main research interests include motion planning and control of microaerial vehicles.